ESC European Society of Cardiology

Cardiovascular Research (2022) **118**, 798–813
doi:10.1093/cvr/cvab126

Novel insights into the electrophysiology of murine cardiac macrophages: relevance of voltage-gated potassium channels

Ana Simon-Chica [1,2], Marbely C. Fernández[1], Eike M. Wülfers [1], Achim Lother [3,4], Ingo Hilgendorf[3], Gunnar Seemann [1], Ursula Ravens[1], Peter Kohl[1], and Franziska Schneider-Warme [1,*]

[1]Institute for Experimental Cardiovascular Medicine, University Heart Center Freiburg - Bad Krozingen, Faculty of Medicine, University of Freiburg, Elsaesser Str. 2Q, 79110 Freiburg, Germany; [2]Centro Nacional de Investigaciones Cardiovasculares, Carlos III (CNIC), Myocardial Pathophysiology Area, Melchor Fernández Almagro 3, 28029 Madrid, Spain; [3]Department of Cardiology and Angiology I, University Heart Center Freiburg - Bad Krozingen, Medical Center—University of Freiburg, Faculty of Medicine, University of Freiburg, Hugstetter Str. 55, 79106 Freiburg, Germany; [4]Institute of Experimental and Clinical Pharmacology and Toxicology, Faculty of Medicine, University of Freiburg, Albertstr. 25, 79104 Freiburg, Germany

Received 13 July 2020; editorial decision 24 March 2021; accepted 5 April 2021; online publish-ahead-of-print 6 April 2021

Time for primary review: 47 days

Aims Macrophages (MΦ), known for immunological roles, such as phagocytosis and antigen presentation, have been found to electrotonically couple to cardiomyocytes (CM) of the atrioventricular node *via* Cx43, affecting cardiac conduction in isolated mouse hearts. Here, we characterize passive and active electrophysiological properties of murine cardiac resident MΦ, and model their potential electrophysiological relevance for CM.

Methods and results We combined classic electrophysiological approaches with 3D florescence imaging, RNA-sequencing, pharmacological interventions, and computer simulations. We used $Cx_3cr_1^{eYFP/+}$ mice wherein cardiac MΦ are fluorescently labelled. FACS-purified fluorescent MΦ from mouse hearts were studied by whole-cell patch-clamp. MΦ electrophysiological properties include: membrane resistance 2.2±0.1 GΩ (all data mean±SEM), capacitance 18.3±0.1 pF, resting membrane potential -39.6±0.3 mV, and several voltage-activated, outward or inwardly rectifying potassium currents. Using ion channel blockers (barium, TEA, 4-AP, margatoxin, XEN-D0103, and DIDS), flow cytometry, immuno-staining, and RNA-sequencing, we identified Kv1.3, Kv1.5, and Kir2.1 as channels contributing to observed ion currents. MΦ displayed four patterns for outward and two for inward-rectifier potassium currents. Additionally, MΦ showed surface expression of Cx43, a prerequisite for homo- and/or heterotypic electrotonic coupling. Experimental results fed into development of an original computational model to describe cardiac MΦ electrophysiology. Computer simulations to quantitatively assess plausible effects of MΦ on electrotonically coupled CM showed that MΦ can depolarize resting CM, shorten early and prolong late action potential duration, with effects depending on coupling strength and individual MΦ electrophysiological properties, in particular resting membrane potential and presence/absence of Kir2.1.

Conclusion Our results provide a first electrophysiological characterization of cardiac resident MΦ, and a computational model to quantitatively explore their relevance in the heterocellular heart. Future work will be focussed at distinguishing electrophysiological effects of MΦ–CM coupling on both cell types during steady-state and in patho-physiological remodelling, when immune cells change their phenotype, proliferate, and/or invade from external sources.

* Corresponding author. Tel: +49 76127063954; fax: +49 76127063959, E-mail: Franziska.Schneider.uhz@uniklinik-freiburg.de

Graphical Abstract

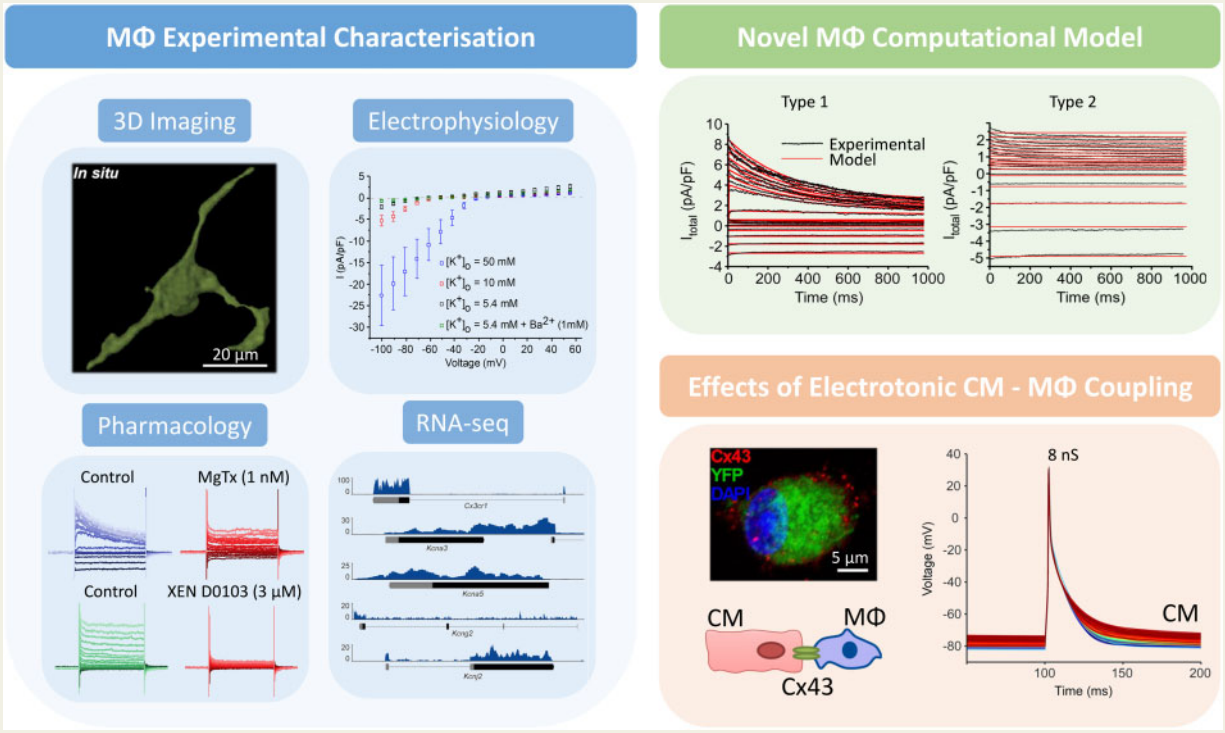

Keywords Cardiomyocytes • Heterocellular electrotonic coupling • Connexin-43 • Electrophysiology • Inward-rectifier K^+ channel • Outward K^+ channel

1. Introduction

Cardiac contraction drives blood flow, based on coordinated electrical activation of cardiomyocytes (CM) through a propagating wave of action potentials (AP). CM are surrounded by non-myocytes, such as fibroblasts and myeloid cells including resident macrophages (MΦ). There are more non-myocytes than CM in healthy myocardium,[1,2] and their numbers increase following injury.[3]

MΦ play important roles for tissue maintenance and during inflammation, as they recognize, engulf and destroy target cells or cell debris. The majority of cardiac MΦ in healthy mammalian hearts are tissue resident, embryonically derived cells, whereas bone marrow-derived MΦ contribute in particular post-injury.[4] Resident MΦ promote cardiac tissue healing and homoeostasis,[5,6] and disturbances in cardiac MΦ function can lead to abnormal repair, involving release of inflammatory cytokines, and growth factors.[3]

In addition to immunological functions and roles in clearing subcellular particles shed by CM as part of their structural homoeostasis,[7] resident cardiac MΦ appear to fulfil distinct 'non-canonical' roles. Thus, MΦ can be electrotonically coupled *via* Connexin-43 (Cx43) to CM of the atrioventricular node of mice.[8] Using optogenetic targeting to depolarize MΦ, or cell-type specific Cx43 deletion, Hulsmans *et al.*[8] showed that resident MΦ can alter the electrophysiology of CM, affecting atrioventricular conduction in isolated mouse hearts.

The electrophysiological properties of cardiac MΦ are ill-explored. In contrast, the electrical behaviour of cardiac fibroblasts, and their coupling to CM, have been studied from as early as 1969, when fibroblast-mediated AP conduction between otherwise unconnected CM was shown *in vitro*.[9] In 1992, Rook *et al.*[10] characterized cardiac fibroblast electrophysiology and Cx-mediated coupling to CM in isolated cell pairs, and in 2016 Quinn *et al.*[11] confirmed that non-myocytes can be electrotonically linked to CM in scar border tissue of Langendorff-perfused murine whole hearts. Computational models have been used to explore potential electrophysiological effects of CM-fibroblast coupling *in silico*.[12–15] By assessing the quantitative plausibility of hypotheses, these models can complement wet-lab experimentation, though no MΦ model is available at this time.

Here, we present first insights into cardiac resident MΦ electrophysiology, and explore their potential interactions with CM using a computational model. Electrophysiological characterization includes passive (membrane resistance, membrane capacitance, resting membrane potential [RMP]), and active properties (voltage-activated outward and inwardly rectifying currents). Using ion channel blockers, RNA-sequencing (RNA-seq), and flow cytometry, we identify major voltage-gated potassium (K^+) channels underlying MΦ electrical behaviour as Kv1.3, Kv1.5, and Kir2.1. On this basis, we developed a computational model to describe the electrophysiological behaviour of murine cardiac MΦ. The model reproduces experimental observations and is used to predict effects of electrotonic MΦ–CM coupling: MΦ depolarize the RMP of CM (by up to 9.4 mV), shorten early and prolong late AP duration (by up to -34.9% at 50% repolarization, and +12.7% at 90% repolarization, depending on coupling strength and ion channels expressed in MΦ).

Our work establishes the basis for further quantitative research into MΦ electrophysiology and heterocellular interactions with CM. In the future, we aim to extend this research from cellular properties and interactions in steady-state to patho-physiological changes, when immune cells alter their phenotype, proliferate, and/or invade from extra-cardiac sources.

2. Methods

2.1 Mouse lines used

All animal experiments were carried out according to the guidelines in Directive 2010/63/EU of the European Parliament on the protection of animals used for scientific purposes; they were approved by local authorities in Baden–Württemberg, Germany (X19/01R).

B6.129P2(Cg)-*Cx$_3$cr$_1^{tm2.1(cre/ERT2)Litt}$*/WganJ mice (Cx$_3$cr$_1^{eYFP/+}$; JAX stock #021160) wherein enhanced yellow fluorescent protein (eYFP) is expressed under the control of the fractalkine Cx$_3$cr$_1$ promoter were used for this study, unless otherwise stated.[16] Experimental mice were 8–12 weeks old, and age-matched litter mates not expressing eYFP served as controls.

For MΦ–CM and ion channel co-localization studies (see Supplementary Methods as well as *Figures S4 and S5*), we used B6.129P2(C)-*Cx$_3$cr$_1^{tm2.1(cre/ERT2)Jung}$*/J mice (Cx$_3$Cr$_1^{CreERT2}$; JAX stock #020940)[17] cross-bred with B6;129S-*Gt(ROSA)26Sor$^{tm32(CAGCOP4*H134R/EYFP)Hze}$*/J mice (Cre-dependent Channelrhodopsin-2-eYFP strain, JAX stock #012569)[18] to allow MΦ surface visualization. Expression of Cre recombinase was induced by injection of tamoxifen (3 mg intraperitoneally on five consecutive days between P42 and P56), as previously described.[19]

2.2 Macrophage isolation

Mice were euthanized by cervical dislocation. Hearts were swiftly excised and gently flushed with 20 mL of cold phosphate buffered saline (PBS). Thereafter, tissue was minced into small pieces and subjected to enzymatic digestion with 450 U/mL collagenase I, 125 U/mL collagenase XI, 60 U/mL DNase I, and 60 U/mL hyaluronidase (all Sigma-Aldrich, Munich, Germany) in 1 mL PBS for 35 min at 37°C under gentle agitation. Tissue fragments were then triturated, filtered through a 40-μm nylon mesh (Thermo Fisher Scientific, Waltram, MA, USA), and pelleted by centrifugation (400×*g* for 5 min at 4°C). Cells were re-suspended in fluorescence-activated cell sorting (FACS) buffer (PBS with 1% foetal calf serum + 0.1% bovine serum albumin).

Cardiac MΦ were FACS-purified using an Aria III cell sorter (BD Biosciences, Franklin Lakes, NJ, USA). Cells from YFP$^-$ littermates were used as negative controls. Cellular identity was validated using additional antibody staining that identified resident murine cardiac MΦ as YFP$^+$ CD45$^+$ CD11b$^+$ F4/80$^+$ Ly6C$^-$. MΦ -were further separated into two groups, based on their relative expression level of MHC-II (Supplementary *Figure S2*). FlowJo software was used to analyse FACS data.

2.3 Cell culture

FACS-purified MΦ were seeded onto coverslips in 24-well plates at a final density of 20,000 cells/mL in 1 mL Dulbecco's Modified Eagle Medium (Thermo Fisher Scientific), supplemented with 10% heat-inactivated foetal calf serum and 1% penicillin/streptomycin (all Sigma-Aldrich). Non-adherent cells were removed by changing medium before functional experiments. If not stated otherwise, experiments were performed 15–30 h post-isolation. Passive electrophysiological properties of MΦ were additionally determined at a second point in time, after 7 days in culture.

2.4 Whole-cell patch-clamp

Patch-clamp measurements on isolated MΦ were performed at room temperature using an inverted DMI 4000B microscope (Leica Microsystems, Wetzlar, Germany), a patch-clamp amplifier (200B, Axon Instruments, FosterCity, CA, USA), and a Digidata 1440A interface (Axon Instruments). Patch-clamp electrodes were made with a micropipette puller (PP-830, Narishige, Tokyo, Japan) from filamented borosilicate glass capillaries (160213 BRIS, ISO12772, Vitrex Medical A/S, Vasekaer, Denmark). Pipette tip resistance was 2.0–4.0 MΩ when filled with pipette solution.

During whole-cell patch-clamp recordings, the extracellular (bath) solution consisted of (in mM): 5.4 KCl, 150 NaCl, 10 HEPES, 2 $MgCl_2$, 10 Glucose, and 2 $CaCl_2$ (pH 7.4; adjusted to 300±5 mOsm with glucose). Pipette solution contained (in mM): 8 NaCl, 40 KCl, 80 K-Aspartate, 2 $CaCl_2$, 0.1 Tris-GTP, 5 Mg-ATP, 5 EGTA, and 10 HEPES (pH 7.4; adjusted to 300 ± 5 mOsm with D-mannitol).

For pharmacological identification of ion channels, the following blockers were diluted in bath solution and applied using a custom-built solution exchanger: Barium ($BaCl_2$; 1 mM), tetraethylammonium (TEA; 1 mM), 4-aminopyridine (4-AP; 1 mM), 4,4'-diisothiocyano-2,2'-stilbenedisulfonic acid (DIDS; 100 μM; all Sigma-Aldrich), recombinant margatoxin (MgTx; 1 and 10 nM; Alomone Labs, Jerusalem, Israel), or XEN-D0103 (3 μM; Xention Ltd, Cambridge, UK, kindly provided by Metrion Biosciences Ltd, Cambridge, UK). $BaCl_2$, TEA, 4-AP, DIDS, and XEN-D0103 (10 mM in DMSO) were dissolved at their target concentration in bath solution and supplied as bulk perfusate. MgTx was reconstituted at a concentration of 10 μM in Tris buffer (0.1% bovine serum albumin, 100 mM NaCl, 10 mM Tris, pH 7.5) and added locally at the target concentration to the non-perfused bath.

Recordings were corrected for liquid junction potentials. Data analysis was performed using a custom-developed Matlab script (available from the authors on request). The voltage dependence of activation was analysed using two protocols: (i) voltage pulse, where cells were polarized for 1 s from a holding potential of –60 mV to a range of potentials between –100 and +60 mV, in 10 mV increments (square pulses with an inter-pulse duration of 5 s), and (ii) a voltage ramp from –80 to +50 mV, applied as a linear increment over 2.2 s. Peak currents in the pulse protocol were normalized to maximum peak current observed and plotted against voltage. Cumulative inactivation of outward currents (as reported previously)[20] was measured by applying a train of 10 repetitive 200 ms voltage steps from a holding potential of –60 to +50 mV (square pulses with an inter-pulse duration of 1 s). The amount of cumulative inactivation was calculated as the percentage of each successive current amplitude, relative to the peak current during the first pulse.

To unravel kinetic properties of different currents, experiments were performed to acquire steady-state activation and inactivation data. For steady-state activation, we used the pulse protocol described, and the conductance *g* was calculated from:

$$g = \frac{I_{peak}}{(V - E_{rev})}, \quad (1)$$

where I_{peak} is the peak current, and E_{rev} is the reversal potential. The conductance–voltage curves of activation were fitted with a Boltzman equation as:

$$\frac{g}{g_{max}} = \frac{1}{1 + \exp\left(-\frac{(V - Va_{50})}{k}\right)}, \quad (2)$$

where g_{max} is the maximum conductance, Va_{50} is the voltage of half maximal conductance during current activation, and k is the slope factor.

For steady-state inactivation, membrane potentials were clamped at levels between –80 and –10 mV for at least 30 s, followed by a 1-s depolarizing step to +60 mV. The steady-state inactivation curve was fitted to the following Boltzmann equation:

$$\frac{I}{I_{max}} = \frac{1}{1 + \exp\left(\frac{(V - Vi_{50})}{k}\right)}, \quad (3)$$

where I_{max} is the maximum peak current, Vi_{50} is the potential at which peak current is inactivated by 50%, and k is the slope factor.

The time constants of activation and inactivation (τ_{act} and τ_{inact}, respectively) were analysed using the same step protocol, fitting experimental current traces as a function of time $I_{exp}(t)$ with the following double-exponential formula:

$$I_{exp}(t) = a \cdot \left(1 - \exp\left(\frac{-t}{\tau_{act}}\right)\right) + b \cdot \exp\left(\frac{-t}{\tau_{inact}}\right) + c \quad (4)$$

where t refers to experimental time, and a, b, and c are constants.

2.5 RNA-seq and bioinformatics analysis

Total RNA was isolated from purified cells using an AllPrep DNA/RNA Micro Kit (Qiagen, Hilden, Germany). RNA-seq libraries were prepared from 5 ng RNA per sample using the Ovation SoLo RNA-seq System (NuGEN, Redwood City, CA, USA). cDNA fragments of ~350 bp were obtained by sonication (Bioruptor, Diagenode, Liège, Belgium), fluorescence-controlled PCR amplification, and size selection using AMPure XP Beads (Beckmann Coulter, Brea, CA, USA). Quality and mean fragment size of library samples were assessed using a Bioanalyzer (2100 Bioanalyzer, Agilent Technologies, Santa Clara, CA, USA), and libraries were sequenced on Illumina sequencers in paired-end mode.

Sequencing data were analysed using the Galaxy platform.[21] RNA-seq reads were trimmed and mapped to the *Mus musculus* genome (NCBI37/mm9) using STAR.[22] After duplicate removal, transcript abundance was estimated as fragments per kilobase of transcript per million fragments, mapped using Cufflinks.[23]

2.6 Immunocytochemistry

For immunocytochemistry, cells were fixed on coverslips using 4% paraformaldehyde in PBS (pH 7.4) for 10 min, permeabilized with PBS containing 0.3% Triton X-100 for 10 min, and washed in PBS. Blocking solution (PBS + 0.1% Tween-20 + 10% foetal calf serum) was applied for 1 h. The primary rabbit-anti-Cx43 antibody (1:400, Abcam, Cambridge, UK) was dissolved in antibody diluent solution consisting of 0.02% Triton-X, 1% bovine serum albumin, and 2.5% goat serum in PBS, and cells were incubated overnight at 4°C. Subsequently, samples were incubated with the fluorochrome-labelled secondary Alexa Fluor 647 goat-anti-rabbit IgG, 1:1,000 (Thermo Fisher Scientific) for 2 h at room temperature, and Hoechst 33342 nuclear counterstain (1:1,000, Thermo Fisher Scientific) was added for 5 min at room temperature (all antibodies listed in Supplementary *Table S1*, all incubation conducted in the dark). Cells were washed in PBS three times for 10 min and mounted in PermaFluor aqueous mounting medium (Thermo Fisher Scientific).

2.7 Indirect flow cytometry

Rabbit-anti-K_v1.3, anti-K_v1.5, anti-K_{ir}2.1 primary antibodies (1:500; all from Alomone Labs), or rabbit-anti-Cx43 antibody (1:400, Abcam ab11370) were added to the cell suspension and incubated for 30 min at 4°C. Cells were washed three times by centrifugation (400 x g for 5 min at 4° C) and the secondary antibody (as above) was added to the cell suspension. After 20-30 min of incubation at 4°C, cells were washed three times by centrifugation and re-suspended in FACS buffer. Data were collected on a BD FACS Canto II (BD Bioscience, San Diego, CA, USA) and analysed with FlowJo.

2.8 Confocal microscopy of immunolabelled cells

Fluorescence images were acquired on an inverted confocal microscope (TCS SP8 X, Leica Microsystems, Wetzlar, Germany) using a water immersion objective (HC PL APO 40×). The different fluorophores were excited using either a 405 nm diode laser or appropriate 'lines' (i.e. 1–3 nm narrow bands) from a white light laser. The different fluorescence signals were recorded with suitable spectral detection windows. A photomultiplier tube detector was used for recording the Hoechst 33342 signal and more sensitive hybrid detectors for all other fluorescence channels. Imaging was performed using the Leica LIGHTNING module, which offers deconvolution-based super-resolution.

2.9 X-Clarity

Whole mouse hearts (N=3) were excised as described above and immediately Langendorff-perfused with 10 mL of Tyrode solution, followed by 10 mL 4% paraformaldehyde in PBS. Hearts were stored in 4% paraformaldehyde for 5 h at 4°C, then washed three times with PBS, and stored in PBS overnight at 4°C before being cleared (X-CLARITY, Logos Biosystems, USA). The clearing process followed X-CLARITY instructions for mouse brain. The heart was polymerized for 3 h at 37°C in -90 kPa vacuum, agitated for 1 min, and rinsed with electrophoretic tissue clearing solution. Subsequently, hearts were incubated for 12 h at 37°C in the electrophoresis chamber with electrophoretic tissue clearing solution, while applying a current of 1.0 A. For immuno-staining, cleared hearts were incubated for 1 day at 37°C in blocking solution (0.5% Triton-X, 2.5% bovine serum albumin and 5% goat serum).

A primary rabbit-anti-GFP antibody that binds to eYFP was added and incubated for 2 days at 37°C (Abcam, 1:800 in antibody diluent solution containing 0.05% NaN_3). The primary antibody was washed off with PBS containing 0.1% Tween for one day. The secondary goat-anti-rabbit Alexa 488 antibody (Thermo Fisher Scientific; 1:1,000 in antibody diluent solution) was applied for 2 days at 37°C. Unbound secondary antibody was washed off as above. Then, cleared hearts were incubated for 5 h at 37°C with Hoechst 33342 nuclear counterstain (1:500), washed off in PBS for 1 day.

For imaging, cleared hearts were washed with distilled water prior to immersion in X-CLARITY mounting solution for 2 h. Hearts were then transferred to a 35 mm µ-dish (Ibidi, Gräfelfing, Germany) containing fresh mounting solution. Imaging was performed as explained in the previous section.

2.10 3D reconstruction

3D reconstructions of MΦ were created semi-automatically using custom software written in Python (code available from the authors upon request). Raw images were loaded into numpy arrays using the tifffile library. Each channel was filtered with a Gaussian filter kernel (σ=1 voxel)

using the *ndimage* module from SciPy. Background was removed from each channel by subtracting from each voxel the mode of the intensity histogram, and by setting any resulting negative values to 0. Depth-dependent attenuation was corrected in each channel by fitting an exponential function to average intensities of each slice and scaling the intensities by the inverse of the resulting function. Next, binary segmentations were created as foundation for the 3D reconstructions using a threshold (T), based on the average (Avg) and standard deviation (SD) of the intensity per channel: $T = \text{Avg} + f_{SD} \times \text{SD}$ for MΦ-specific fluorescence, and $T = \text{Avg} + 2\ \text{SD}$ for nuclei stain. The value for f_{SD} was chosen between 1.75 and 3, based on visual inspection of image quality. Five iterations of binary dilation, followed by five iterations of binary closing were performed on MΦ segmentations using an ellipsoidal structural element with axis length of 2 voxels in x- and y-directions and 1 voxel in z-direction. Four iterations of binary erosion were performed on each slice for nuclei segmentations, followed by three iterations of binary closing, using the same structuring element as for MΦ.

Contiguous objects in the binary MΦ and nuclei stain segmentations were uniquely labelled, and objects with a size of <2,000 voxels were removed to eliminate small artefacts. Voxel sizes of 3D reconstruction from fresh, cultured and, *in situ* MΦ are shown in Supplementary *Table S2*. The scikit-image library was used for these operations.[24] Objects in MΦ segmentations touching stack boundaries were removed to exclude incompletely imaged cells in later analyses.

For each of the segmented nuclei, co-localization with any object in the MΦ segmentations was determined. If co-localized voxels were <Z% of the total number of voxels of a segmented nucleus, that nucleus was considered as belonging to a neighbouring (non-MΦ) cell. Z was chosen between 10 and 25, based on visual assessment of the nuclei segmentations. The low-percentage cut-off results from the fact that co-localization occurs only at the surface of nuclei.

MΦ and nuclei segmentations were merged and binarized, as nuclei could theoretically connect previously unconnected objects.

A Gaussian filter with σ=2 voxels in x- and y-directions and 0.5 voxels in z-direction was applied, followed by one iteration of grey dilation with a box structuring element of 15×15×5 voxels. This created monotonically decreasing intensities from the inside towards the outside of each cell that could be used to adjust over-/under-segmentation when creating 3D surfaces. An iso-surface threshold, chosen based on image quality between 80 and 180 (out of 255), was used when computing surfaces, using a marching cubes algorithm[25] implemented in scikit. The resulting triangular mesh was further processed and analysed using the open-source Visualization Toolkit.[26] First, a smoothing filter (*vtkSmoothPolyDataFilter*) was applied to the mesh with 3,000 iterations, a convergence threshold of 0.1, and a feature angle of 90°. Volumes and surface areas of each of the resulting 3D reconstructions were computed using the *vtkMassProperties* filter.

2.11 Statistical analysis

Data distribution was assessed with the Shapiro–Wilk normality test. Normally distributed data were compared by one-way ANOVA. Non-normally distributed data were compared with the Mann–Whitney U test. Data were expressed as mean±SEM, and P-values <0.05 were considered as indicative of statistically significant differences between means (*P<0.05; **P<0.001, ***P<0.0001). In addition, a linear mixed-effects model was fitted to account for data clustering linked to individual mice used. Commonly used aforementioned statistical tests and hierarchical models were compared. Throughout the study, n/N refers to the number of cells/hearts (biological replicates).

2.12 MΦ model development

A computational model was developed to describe passive and active electrophysiological properties of murine cardiac MΦ, based on original whole-cell patch-clamp data. The model includes two time- and voltage-dependent outward K^+ currents, an inwardly rectifying K^+ current, as well as a non-selective background current. The default membrane capacitance $C_{M\Phi}$ was set to the mean of measured membrane capacitances (18.3 pF; n=142 MΦ, N=32 hearts). Full details of the mathematical formulations for each current are disclosed in the Supplementary Methods. In short, the time- and voltage-dependent outward current $I_{Kv1.3}$ is described as a shaker current. Our experimental data confirm that this current belongs to the Kv1.3 family. To this end, we optimized a 7-state Markov model (developed originally for shaker channels in T lymphocytes)[28] with five closed (C_0,. . .,C_4), one open (O), and one inactivated (I) state (Supplementary *Figure S1*). The voltage-gated Kv1.5 channel mediating the ultrarapid K^+ current is derived from a previous model[29] and parametrized based on our experimental data. The inwardly rectifying K^+ current is described by re-parametrizing a model previously used for I_{K1} in CM.[27] The background current is an unspecific, electrotonic background current that was added to the model using the formulation of previous Ohmic models in cardiac fibroblasts.[15]

The integration of voltage-clamp data into the model was carried out by a trust region reflective optimization algorithm. To this end, we used the Matlab function *lsqnonlin* to constrain the solution space for model parameters in a defined range (0.01×, 100×). Constants after optimization for each MΦ current profile, and physical constants used in the model are summarized in Supplementary *Tables S3 and S4*.

Building on this default model description, a population of models approach was developed that explores the impact of variable MΦ phenotypes on CM cross-talk. To construct the population of models, the conductance of the four ion currents included in the model and $C_{M\Phi}$ were varied systematically from 50% to 200% of their original value. A total number of 400 different combinations of the aforementioned parameters were generated using Latin Hypercube Sampling[30] (Supplementary Methods).

2.13 Modelling heterocellular coupling

MΦ–CM interactions were investigated using the above MΦ models and a mouse CM model.[31] Heterocellular coupling was introduced using linear resistive coupling. The intercellular 'gap junction' current I_{gj} provides electrotonic coupling between two cells as in:

$$I_{gj} = g_{gj}(V_{m,2} - V_{m,1}), \tag{5}$$

where g_{gj} is the gap-junctional conductance (assumed to be Ohmic), and $V_{m,x}$ is the transmembrane voltage in cell x.

By introducing this term into the reaction–diffusion equations, transmembrane voltage for connected cells is:

$$C_{m,1}\frac{dV_{m,1}}{dt} = I_{ion,1} - I_{gj}, \tag{6}$$

$$C_{m,2}\frac{dV_{m,2}}{dt} = I_{ion,2} + I_{gj}, \tag{7}$$

where $I_{ion,x}$ is the transmembrane current and $C_{m,x}$ the membrane capacitance of cell x.

To quantify the impact of different MΦ subtypes on RMP and AP characteristics of CM, a single CM model was connected to models of different cardiac MΦ. Intercellular g_{gj} was set to 0, 1, 2 or 8 nS to represent no coupling, weak, medium, and high coupling, respectively. The CM was

stimulated at 5 Hz for 10 s to approach steady-state. Simulations were implemented in Myokit[32] and ordinary differential equations were solved using the forward Euler method with a time step of 5 μs.

3. Results

3.1 Cardiac MΦ isolation and passive properties

Cx_3cr_1 MΦ were isolated from cardiac cell suspensions of healthy $Cx_3cr_1^{eYFP/+}$ mice comprising a major $Ly6C^{low}$ MHC-II^{high} (63%) and a minor $Ly6C^{low}$ MHC-II^{low} population (15%; all percentages with reference to $eYFP^+$ cells; Supplementary *Figure S2*), as previously described.[33,34] In control samples from $Cx_3cr_1^{eYFP/-}$ littermates, fewer than 0.003% of cells were false-positively FACS-sorted as $eYFP^+$.

Figure 1A shows representative confocal images of cardiac MΦ and their 3D reconstructions for freshly isolated, cultured (1 week), and *in situ* cells. After isolation, cardiac MΦ are near-spherical. Cultured MΦ are larger, with elongated cellular processes. MΦ *in situ* present multiple cytoplasmic projections. The surface membrane area of freshly isolated MΦ is 379±22 μm^2 (n=21 cells, N=3 hearts). This is significantly smaller than the surface area of cultured (841±103 μm^2; n=14, N=3) or *in situ* cardiac MΦ (1,163±81 μm^2; n=35, N=3; right panel in *Figure 1B*).

Passive electrophysiological properties of freshly isolated cardiac MΦ include a membrane resistance of 2.21±0.07 GΩ (n=142, N=32) and a capacitance of 18.3±0.1 pF (n=142, N=32). RMP, measured immediately after obtaining the whole-cell configuration, was -39.6±0.3 mV (n=63, N=23; *Figure 1B*). In keeping with the increase in surface area, MΦ cultured for 1 week had a larger capacitance of 34±0.4 pF (n=35; N=2) and a lower membrane resistance of 1.12±0.03 GΩ (n=15, N=2). RMP was not statistically different after 1 week in culture, at -42.2±2.0 mV (n=9, N=2).

3.2 K^+ selectivity of transmembrane currents in cardiac MΦ

To identify the nature of ion currents in MΦ, we varied extracellular ion concentrations and compared changes in E_{rev} with theoretical predictions (Nernst's equation). *Figure 1C* shows I–V curves and representative current traces at extracellular K^+ concentrations ($[K^+]_o$) of 5.4, 10, and 50 mM; currents normalized to cell capacitance (pA/pF) to account for MΦ size. Upon raising $[K^+]_o$, inwardly directed currents with increased amplitude appear at holding potentials negative to E_{rev} (*Figure 1C*); these can be inhibited by 1 mM $BaCl_2$. When changing $[K^+]_o$ from 5.4 to 50 mM, E_{rev} was shifted (in absolute value) by +48±3.8 mV (n=4, N=2), in line with a theoretically predicted shift by +56.6 mV. In contrast, E_{rev} was only marginally depolarized when raising $[Ca^{2+}]_o$ from 2 to 20 mM (observed: +7.1±2.7 mV [n=10, N=2], predicted: +29.3 mV). E_{rev} was not significantly altered by reducing $[Cl^-]_o$ from 163.4 to 13.4 mM (observed: +3.1±0.6 mV [n=8, N=2], predicted: +63.6 mV; *Figure 1D*).

To narrow down the identity of K^+ channels in MΦ, we applied pharmacological agents. Inward currents were inhibited by 80±5% (n=7, N=3) in the presence of $BaCl_2$ (1 mM), a potent blocker of inwardly rectifying K^+ channels (*Figure 1C and E*). The broad-spectrum K^+ channel blockers 4-AP (1 mM) and TEA (1 mM) inhibited outward currents by 32.2±3.1% (n=4, N=3) and 38.6±3.6% (n=9, N=5), respectively. Currents were not affected by the Cl^- channel blocker DIDS (n=7, N=2; *Figure 1E*).

RNA-seq revealed that, among genes encoding channel proteins that conduct K^+ currents, *Kcna3, Kcna5, Kcng2*, and *Kcnj2* are robustly expressed in murine cardiac MΦ (encoding Kv1.3, Kv1.5, Kv6.2, and Kir2.1 channels, respectively) (*Figure 2A* and *Table 1*). Although RNA-seq data show high mRNA levels of genes encoding Ca^{2+} channels, we did not observe any currents indicative of functional expression of voltage-activated Ca^{2+} channels in the plasma membrane of MΦ.

Based on functional and RNA-seq data (*Table 1* and *Figure 2*), we consider Kv1.3 and/or Kv1.5 as plausible substrates for outward, and Kir2.1 for inwardly rectifying K^+ currents observed in cardiac MΦ. RNA-seq data additionally reveal presence of mRNA encoding for Kv6.2 channels; this current was not individually observed in functional studies.

3.3 Electrophysiological heterogeneity of cardiac MΦ

Voltage-dependent currents were variable and cells were classed into eight categories based on the following criteria: (i) outward current magnitude, (ii) threshold of activation, (iii) kinetic properties of inactivation, and (iv) presence of inwardly rectifying current (*Figure 2B*). Cells displaying no apparent voltage-induced activation and only negligible background currents at densities of <1 pA/pF were identified as Type 0 (33.1%, n=47, N=27). Cells with outward currents with an activation threshold near -30 mV that fully activated above 0 mV were identified as Type 1 (14.7%, n=21, N=13). In this group, kinetics of activation and inactivation were voltage-dependent: above 0 mV, outward currents exhibited faster activation and inactivation than below 0 mV. Cells displaying outward currents that gradually increase with depolarization and that do not show apparent inactivation were considered as Type 2 (27.5%, n=39, N=22). Finally, cells where activation at -30 mV was noticeable, but inactivation kinetics were intermediate between Types 1 and 2 were classed as a combination of Types 1 and 2 (24.7%, n=35, N=22).

Each of the aforementioned outward current profiles could appear either in the presence (52.1%) or absence (47.9%) of an inwardly rectifying current (*Figure 1C*). Thus, a total of eight different electrophysiological profiles could be distinguished in murine cardiac MΦ. Note that, up to seven different electrophysiological profiles were found in cells from the same animal (see Supplementary *Figure S3*).

3.4 Kv1.3, Kv1.5, and Kir2.1 channels in cardiac MΦ

To further determine the identity of Kv channels, we tested the peptide MgTx, a potent blocker of Kv1.3 at 1 nM (inhibiting several other Kv channels at 10 nM),[35] and XEN-D0103, which selectively blocks Kv1.5 at 3 μM.[36] Type 0 cells displaying no discernible outward current profiles were excluded from pharmacological experiments.

Figure 3A shows a decrease in maximum current amplitude at +60 mV by 49.5±5.0% in the presence of 1 nM MgTx, and by 59.8±5.6% with 10 nM MgTx (n=12, N=6). Current amplitudes were decreased by 47.6±5.0% in the presence of 3 μM XEN-D0103 (n=7, N=4) (*Figure 3B*), suggesting that Kv1.3 and Kv1.5 channels contribute to observed outward currents. *Figure 3C and D* depict representative voltage-activated currents during voltage ramp protocols in control conditions and during exposure to MgTx (n=15, N=6) or XEN-D0103 (n=8, N=6), leading to similar maximum current inhibition as in voltage step protocols.

To study cumulative inactivation, we analysed responses to repetitive depolarizing pulses from a holding potential of -60 to +50 mV. Type 1 current profiles became progressively smaller (by 63±16% after 10 repeats). This effect was absent in the presence of 1 nM MgTx to block

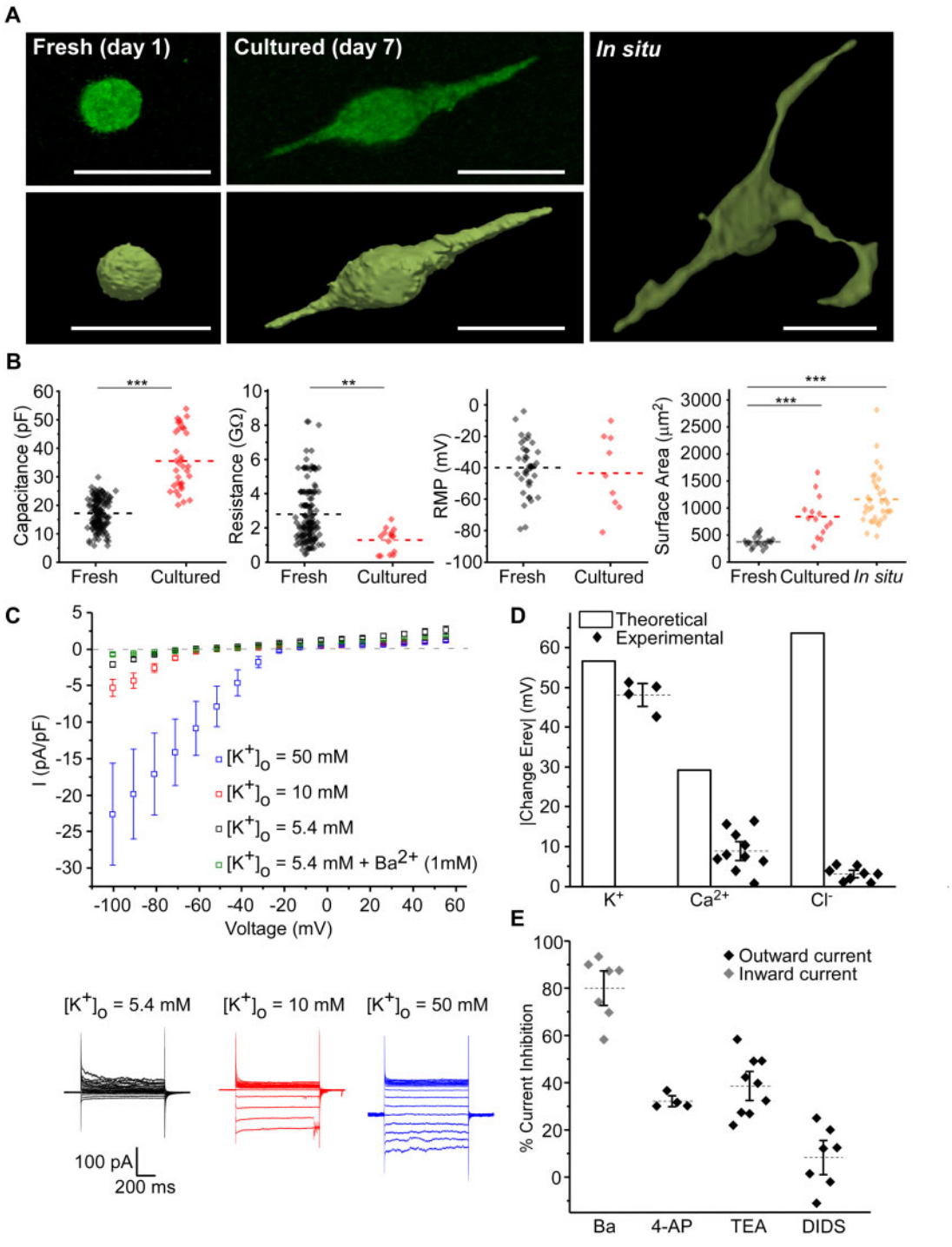

Figure 1 Structural and electrophysiological characterization of murine cardiac MΦ. (*A*) Confocal images (top) and corresponding 3D reconstructions (bottom) of freshly isolated, cultured (7 days), and *in situ* MΦ (imaged after optical clearing of left ventricular tissue). Scale bars 20 μm. (*B*) Comparison of capacitance (n=142MΦ, N=32 hearts [fresh] and n=35, N=2 [cultured]), membrane resistance (n=142, N=32 [fresh] and n=15, N=2 [cultured]), and RMP of freshly isolated and cultured cells (7 days) (n=63, N=23 [fresh] and n=9, N=2 [cultured]). Surface area includes data from *in situ* reconstructions (n=35, N=3). **P<0.001, ***P<0.0001; ANOVA or Mann–Whitney U test and linear mixed model. (*C*) Experimental I–V curves at 5.4 mM (n=8, N=3), 10 mM (n=6, N=3), or 50 mM (n=4, N=2) external potassium ($[K^+]_o$) and after 1 mM $BaCl_2$ application (n=7, N=3) (in presence of 5.4 mM $[K^+]_o$), and representative recordings from a Type 0 MΦ (see *Figure 2*). (*D*) Experimentally observed and theoretically predicted changes (absolute values) in reversal potential, E_{rev}, after varying $[K^+]_o$ from 5.4 to 50 mM (n=4, N=2), extracellular calcium ($[Ca^{2+}]_o$) from 2 and 20 mM (n=10, N=2), or extracellular chloride ($[Cl^-]_o$) from 163.4 to 13.4 mM (n=8, N=2). (*E*) Pharmacological characterization of outward and inward-rectifier currents. Ba^{2+} (1 mM) inhibited inward currents by 80±5% (n=7, N=3). TEA (1 mM, n=9, N=5) and 4-AP (1 mM, n=4, N=3) inhibited outward currents by 38.6±3.6% and 32.2±3.1%, respectively. Currents were not affected by the Cl^- channel blocker DIDS (100 μM; n=7, N=2).

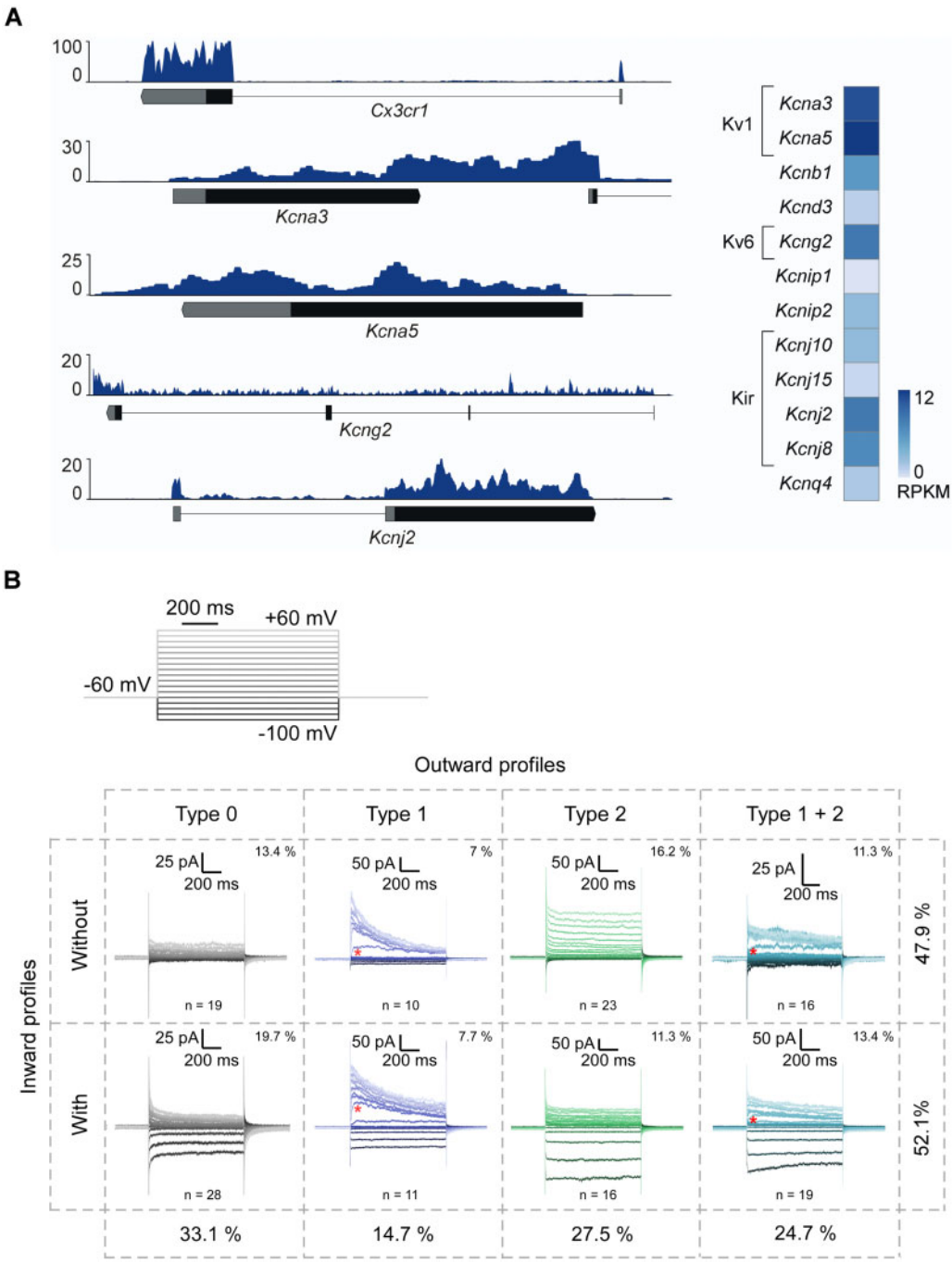

Figure 2 RNA-seq and electrophysiological characterization of murine cardiac MΦ. (*A*) Representative traces and heatmap quantification of RNA-seq data illustrates mRNA expression of *Kcna3* (encoding for Kv1.3), *Kcna5* (Kv1.5), *Kcng2* (Kv6.2), and *Kcnj2* (Kir2.1) in Cx_3cr_1-positive cells (*N*=3 hearts). (*B*) Relative incidence (% of *n*=142 MΦ from *N*=32 hearts) of different outward and inward-rectifier currents in MΦ. Four different patterns for outward currents were identified in cells that either did not (top traces) or did contain prominent inward currents at the most negative polarization steps (bottom traces). Red asterisks show activation threshold near -30 mV found in Type 1 and Type 1+2. The patch-clamp protocol consisted of 1 s voltage steps from a holding potential of -60 mV to potentials from -100 to +60 mV, in 10 mV increments.

Kv1.3 (*Figure 3E*). Unlike Type 1, Type 2 inactivation is slow and does not show cumulative inactivation (*Figure 3F*).

Figure 3G shows representative recordings for voltage-dependent steady-state inactivation for Types 1 and 2 outward current profiles. Type 1 amplitudes decrease with more positive pre-activation voltages. In contrast, Type 2 currents do not completely inactivate during the 30 s pre-activation period, and they show no effect of steady-state voltage on current amplitude. *Figure 3H* presents steady state activation and

Table 1 mRNA expression of ion channels in Cx_3cr_1-positive cells as determined by RNA-seq

Gene identifier	RPKM	Gene identifier	RPKM	Gene identifier	RPKM
Accn2	0.5	Kcna7	0.3	Kcnn2	0.9
Cacna1a	2.8	Kcnb1	5.7	Kcnn3	0.6
Cacna1b	0.4	Kcnb2	0.0	Kcnn4	0.6
Cacna1c	9.4	Kcnc1	0.1	Kcnq1	2.5
Cacna1d	2.9	Kcnc2	0.2	Kcnq2	0.0
Cacna1e	0.0	Kcnc3	0.3	Kcnq3	0.0
Cacna1f	0.1	Kcnc4	0.2	Kcnq4	1.6
Cacna1g	3.0	Kcnd1	0.6	Kcnq5	0.2
Cacna1h	2.4	Kcnd2	0.8	Kcnt1	0.3
Cacna1s	0.1	Kcnd3	1.2	Kcnt2	0.9
Clca1	0.2	Kcnf1	0.1	Kcnu1	0.0
Clca2	0.0	Kcng1	0.1	Kcnv1	0.0
Clca3	0.0	Kcng2	8.2	Kcnv2	0.4
Clca4	0.0	Kcng3	0.0	Orai1	25.1
Clcn1	0.5	Kcng4	0.1	Pkd2	19.0
Clcn2	2.0	Kcnip1	0.2	Scn10a	0.1
Clcn3	14.0	Kcnip2	2.7	Scn11a	0.0
Clcn4-2	15.1	Kcnj1	0.4	Scn1a	0.0
Clcn5	25.2	Kcnj10	2.7	Scn2a1	0.3
Clcn6	7.7	Kcnj11	3.0	Scn3a	0.8
Clcn7	7.8	Kcnj12	1.5	Scn4a	0.9
Fam38a	26.8	Kcnj13	1.2	Scn5a	5.2
Fam38b	0.5	Kcnj14	0.1	Scn7a	6.4
Gja1	34.7	Kcnj15	0.8	Scn8a	0.0
Gja3	0.1	Kcnj16	0.5	Scn9a	0.0
Gja4	4.0	Kcnj2	8.1	Trpa1	0.0
Gja5	2.0	Kcnj3	1.8	Trpc1	0.6
Gja6	0.3	Kcnj4	0.0	Trpc2	9.8
Gjb1	0.0	Kcnj5	1.4	Trpc3	8.7
Gjc1	12.8	Kcnj6	0.0	Trpc4	0.0
Hcn1	0.0	Kcnj8	6.9	Trpc5	0.0
Hcn2	0.7	Kcnj9	0.5	Trpc6	0.3
Hcn3	0.0	Kcnk10	0.0	Trpc7	0.0
Hcn4	0.7	Kcnk2	0.3	Trpm3	1.8
Kcna1	1.4	Kcnk4	0.0	Trpm4	4.2
Kcna10	0.1	Kcnma1	0.5	Trpm7	32.6
Kcna2	0.7	Kcnmb1	0.6	Trpv1	0.3
Kcna3	10.9	Kcnmb2	0.0	Trpv2	17.5
Kcna4	0.1	Kcnmb3	0.0	Trpv4	25.1
Kcna5	12.2	Kcnmb4	0.1		
Kcna6	1.1	Kcnn1	0.5		

RPKM, reads per kilobase per million mapped reads.

inactivation curves for Type 1 currents, plotted against holding potential. The parameters for fitting measured data to Eqs (2)–(4) are summarized in *Table 2*.

Flow cytometry confirmed cell surface expression of Kv1.3 (in 86.0±3.0% of FACS-purified cardiac MΦ), Kv1.5 (84.2±1.8%) and Kir2.1 (55.9±11.8%) (*Figure 3I*; *N*=5). Negative controls (exposed to secondary antibody only) had negligible levels (<0.8±0.2%) of cells false-positively identified as fluorescent, demonstrating appropriate specificity of the approach. The inset in *Figure 3I* shows a representative dot plot where $eYFP^+$ cells were preselected and secondary antibody APC-fluorescence intensity plotted against eYFP fluorescence intensity. HEK-293T cells served as negative control population, since Kv1.3, Kv1.5, and Kir2.1 are not endogenously expressed in HEK cells.

Electrophysiological, RNA-seq and flow cytometry data were confirmed by fluorescence imaging of immuno-labelled ventricular tissue slices, showing consistent presence of Kv1.5, and Kir2.1 channels, co-localized with cardiac MΦ fluorescence (Supplementary *Figures S4 and S5*). Additionally, Cx43 was detected at the interface between CM and MΦ. Kv1.3 could not be observed in tissue-resident MΦ, presumably due to the relatively low expression levels (based on ion current data, fewer than 100 channels would be expected per MΦ).

3.5 Cx43 in cardiac MΦ

To determine whether mouse cardiac MΦ express proteins that may allow electrotonic coupling, the presence of Cx43 in FACS-purified cells was examined. *Figure 3K* illustrates a representative image after immunolabelling that shows punctate staining for Cx43 (in red), preferentially along the MΦ surface. This was confirmed in tissue slices (Supplementary *Figures S4 and S5*).

Flow cytometry detected Cx43 expression in 90.1±1.6% of cardiac MΦ (*N*=4) (*Figure 3J*), while in negative controls (HEK-293T cells, *N*=3) only 2.9±1.7% of cells were false-positively classed as Cx43-expressing. In agreement with immuno-labelling and flow cytometry, RNA-seq data show high transcript levels for Cx43 (*Gja1*, *Table 1*).

In summary, observed biophysical properties including sensitivities to $BaCl_2$, MgTx and XEN-D0103, RNA-seq data, and flow cytometry analysis strongly suggest the functional expression of Kv1.3, Kv1.5, Kir2.1, and the presence of Cx43 in cardiac MΦ. Presumably because of the silent nature of Kv6.2,[37] it was not detected in functional studies.

3.6 Cardiac MΦ computational model

After experimental identification of molecular candidates underlying MΦ currents, a trust region reflective optimization algorithm was implemented for integration of the voltage-clamp data into the MΦ model. Major currents of the model are constituted by an electronic background current I_b, two different time and voltage-dependent outward K^+ currents $I_{outward}$, simulating the Kv1.3/ Kv1.5 (Types I and II outward profiles), and the inwardly rectifying $I_{Kir2.1}$ observed experimentally (*Figure 4A*). Experimental and simulated traces (black and red curves, respectively) demonstrate our ability to reproduce averaged experimental recordings using the MΦ model. *Figure 4B* shows the deconstruction of simulated I–V curves for I_b, the outward currents $I_{Kv1.3}$ (left) or $I_{Kv1.5}$ (right), and the inwardly rectifying $I_{Kir2.1}$ current. *Figure 4C* shows the resulting simulated I–V curve after adding the three corresponding currents represented in *Figure 4B* for each respective outward current profile (Type 1 [left] or 2 [right]).

Figure 5A shows the different combinations of experimentally observed (confer *Figure 2B*) outward and inward-rectifier currents that can be reproduced by the model. MΦ with Type 0 outward current profile correspond to cells showing I_b in the absence or presence of $I_{Kir2.1}$. MΦ with Type 1 outward current profile have an additional current component, which can be modelled by $I_{Kv1.3}$, whereas MΦ with Type 2 outward current profile correspond to cells showing $I_{Kv1.5}$ and I_b in the absence or presence of $I_{Kir2.1}$. MΦ displaying Type 1+2 outward current profile are modelled by combining Types 1 and 2, representing cells expressing

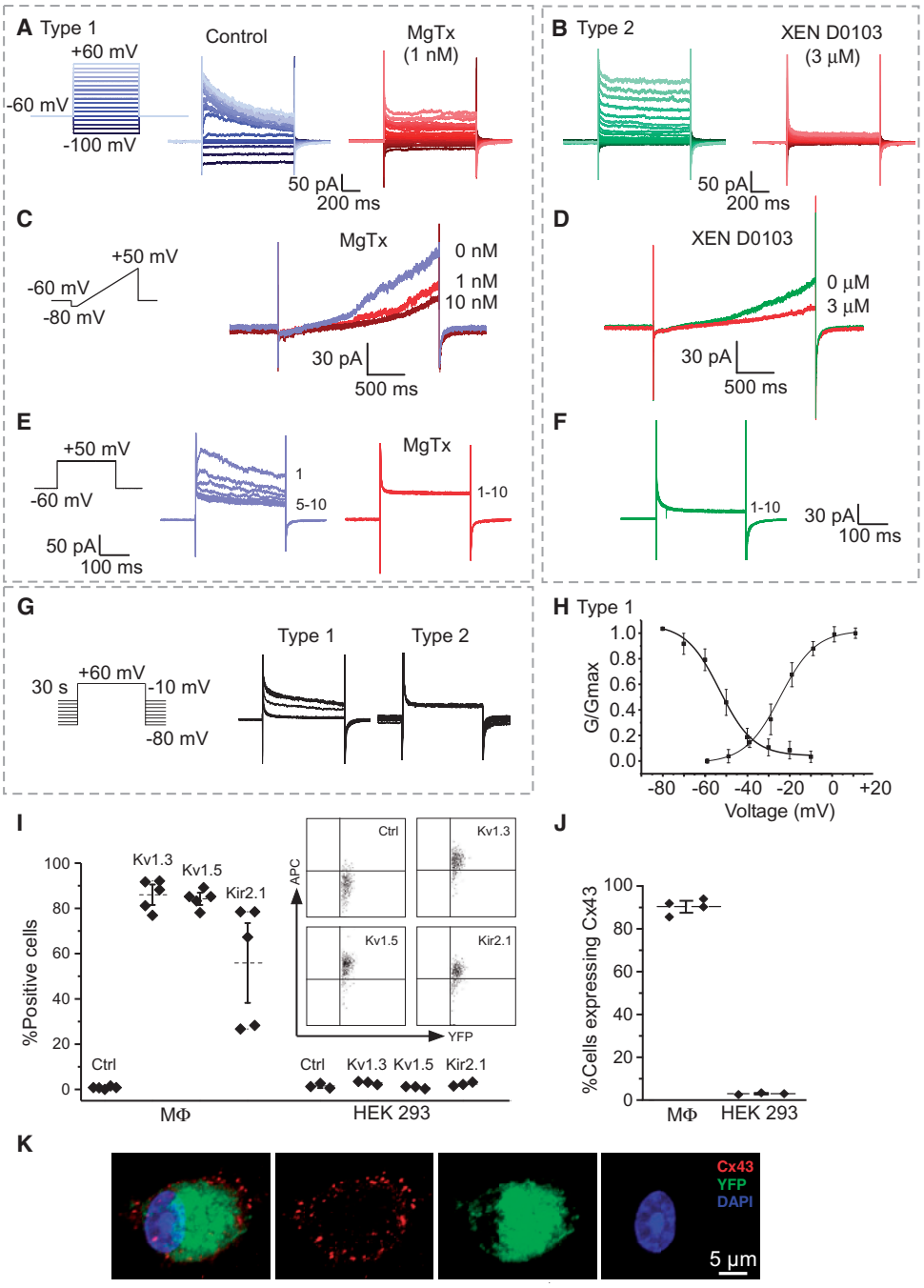

Figure 3 Ion channels in cardiac MΦ. Current inhibition in the presence of 1 and 10 nM MgTx (n=15, N=6) (*A* and *C*) or 3 µM XEN-D0103 (n=8, N=6) (*B* and *D*). (*E*) Cumulative inactivation of Type 1 outward currents was abolished after MgTx application. (*F*) Lack of cumulative inactivation was observed in MΦ with Type 2 outward current profile. (*G*) Representative recordings of steady-state inactivation for Types 1 and 2 outward current profiles. (*H*) Steady-state activation and inactivation curves for Type 1 outward currents plotted as a function of holding potential. (*I*) Flow cytometry quantification of cell surface expression of Kv1.3 (in 86.0±3.0% of FACS-purified cardiac MΦ), Kv1.5 (84.2±1.8%) and Kir2.1 (55.9±11.8%) (N=5); negative control data are from same cells and labels, omitting the primary antibody (<0.8±0.2%). Data from HEK-293T cells (N=3 cultures), which do not endogenously express the ion channels, are shown for comparison. The inset displays representative dot plots where $eYFP^+$ cells were preselected and secondary antibody fluorescence was plotted against eYFP fluorescence intensity. (*J*) Flow cytometry quantification of Cx43 expression in murine cardiac MΦ (N=4) vs. HEK-293T cells (N=3 cultures) as negative control. (*K*) Immuno-labelling of Cx43 of freshly isolated murine cardiac MΦ. Green: eYFP, red: Cx43, blue: nucleus. Scale bar 5 µm.

Table 2 Summary of biophysical properties after fitting experimental data to outward current profiles

Biophysical properties	Type 1 outward current profile
Activation Va_{50} [mV]	-24.8
Steady-state inactivation Vi_{50} [mV]	-48.6
Inactivation time constant [ms]	350
Cumulative inactivation	Yes

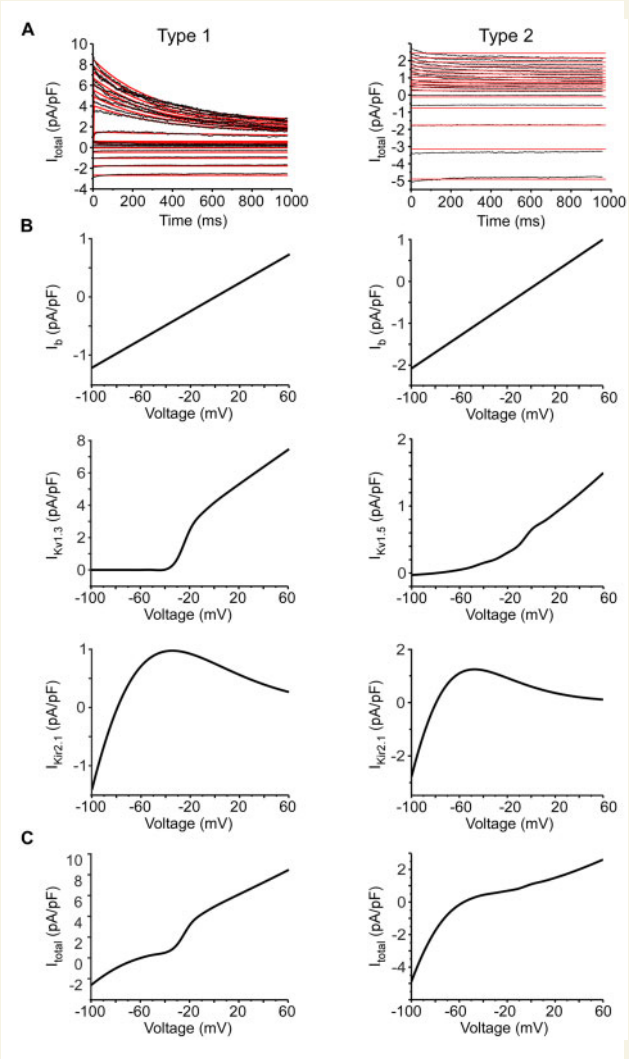

Figure 4 Deconstruction of simulated currents. (*A*) Cardiac MΦ with Type 1 or 2 outward current profiles in the presence of an inward-rectifier current can be reproduced by a background current (I_b), an outward current ($I_{outward}$, $I_{Kv1.3}$ for Type 1, left, or $I_{Kv1.5}$ for Type 2, right) and an inward-rectifier current ($I_{Kir2.1}$). Comparison between simulated (red lines) and experimentally recorded currents (black traces). (*B*) Deconstruction of the different simulated currents. (*C*) Simulated IV curve after adding the three currents represented in (*B*).

both $I_{Kv1.3}$ and $I_{Kv1.5}$ (each individual contribution is optimized to the averaged experimental recording) in the absence or presence of $I_{Kir2.1}$. Without $I_{Kir2.1}$ MΦ RMP values were -10 mV (Type 0), -31.4 mV (Type 1), and -7.6 mV (Type 2). After addition of $I_{Kir2.1}$, these changed to -51.1 mV, -59.7 mV, and -60.7 mV for Types 0, 1, and 2, respectively. RMP of Type 1+2 MΦ was -21 mV, and -60.6 mV in the presence of $I_{Kir2.1}$.

3.7 Effects of MΦ–CM coupling *in silico*

To study the effect of MΦ–CM coupling, a single CM connected to a single MΦ was modelled, while varying the MΦ current profile to represent experimental findings. This configuration was implemented to quantify the impact of MΦ—coupled in 'single-sided' mode[38]—on RMP and AP characteristics of CM, and *vice versa*.

Figure 5B illustrates the principal approach and shows CM membrane voltage (left) during an AP before (0 nS) and after coupling to one MΦ (here of Type 0 in the presence of $I_{Kir2.1}$) at different junctional conductance values, as well as MΦ membrane voltage changes in the same scenario (right).

Based on observed cell-to-cell MΦ variability, a population of models approach was developed and used to explore the impact of 400 variable MΦ phenotypes on MΦ–CM electrophysiological cross-talk (*Figure 6*). In general, MΦ—if they have any discernible effect on coupled CM—will depolarize the RMP of coupled CM (by up to 9.4 mV [from -83.5 mV at 0 nS coupling to maximally -74.1 mV at 8 nS], depending on MΦ model used). This can reduce CM AP upstroke velocity by up to 4.2% (from 275.8 to 264.1 mV × ms^{-1}). In addition, MΦ coupling speeds up early repolarization (shortening APD_{50} by up to 34.9%, from 4.3 to 2.8 ms), and delays late repolarization (prolonging APD_{90} by up to 12.7%, from 74.1 to 83.5 ms) in the most critical scenarios. In turn, CM hyperpolarize coupled MΦ (e.g. for Type 0 + $I_{Kir2.1}$ by up to 27.8 mV, from -51.1 mV at 0 nS coupling to maximally -78.9 mV at 8 nS), and they induce AP-synchronized depolarizations in MΦ.

The effects of MΦ on CM electrophysiology scale with RMP of MΦ. Among the various types of MΦ, the most profound electrotonic cross-talk effects were regularly observed in the absence of the inwardly rectifying $I_{Kir2.1}$ current (Supplementary *Figure S6*). Accordingly, the largest depolarization of CM RMP (by up to 9.4 mV, as mentioned above) was observed when coupling to MΦ presenting Type 2 outward profile in the absence of $I_{Kir2.1}$.

4. Discussion

Advances in cell isolation, flow cytometry, imaging tools, and the development of new genetic reporter lines have helped to provide new insight into phenotypes, subpopulations, and functions of tissue-resident MΦ. Here, we used enzymatic digestion of hearts from $Cx_3cr_1^{eYFP/+}$ mice, followed by flow cytometry, to identify and sort $eYFP^+$ MΦ. We characterized isolated and cultured MΦ functionally and structurally, using single-cell patch-clamp, RNA-seq, immunocytochemistry, and high-resolution 3D fluorescence imaging, also to compare with *in situ* MΦ dimensions. Based on our wet-lab data, we developed a computational model reproducing eight different types of observed MΦ electrophysiology signatures *in silico*. Using a population of models approach, we explored potential effects of CM–MΦ coupling on electrophysiological properties of both cell types.

4.1 Morphology of cardiac MΦ depends on type of experimental model used

We observed significant differences in shape and size of freshly isolated, cultured, and *in situ* ventricular MΦ. While freshly isolated MΦ appear as

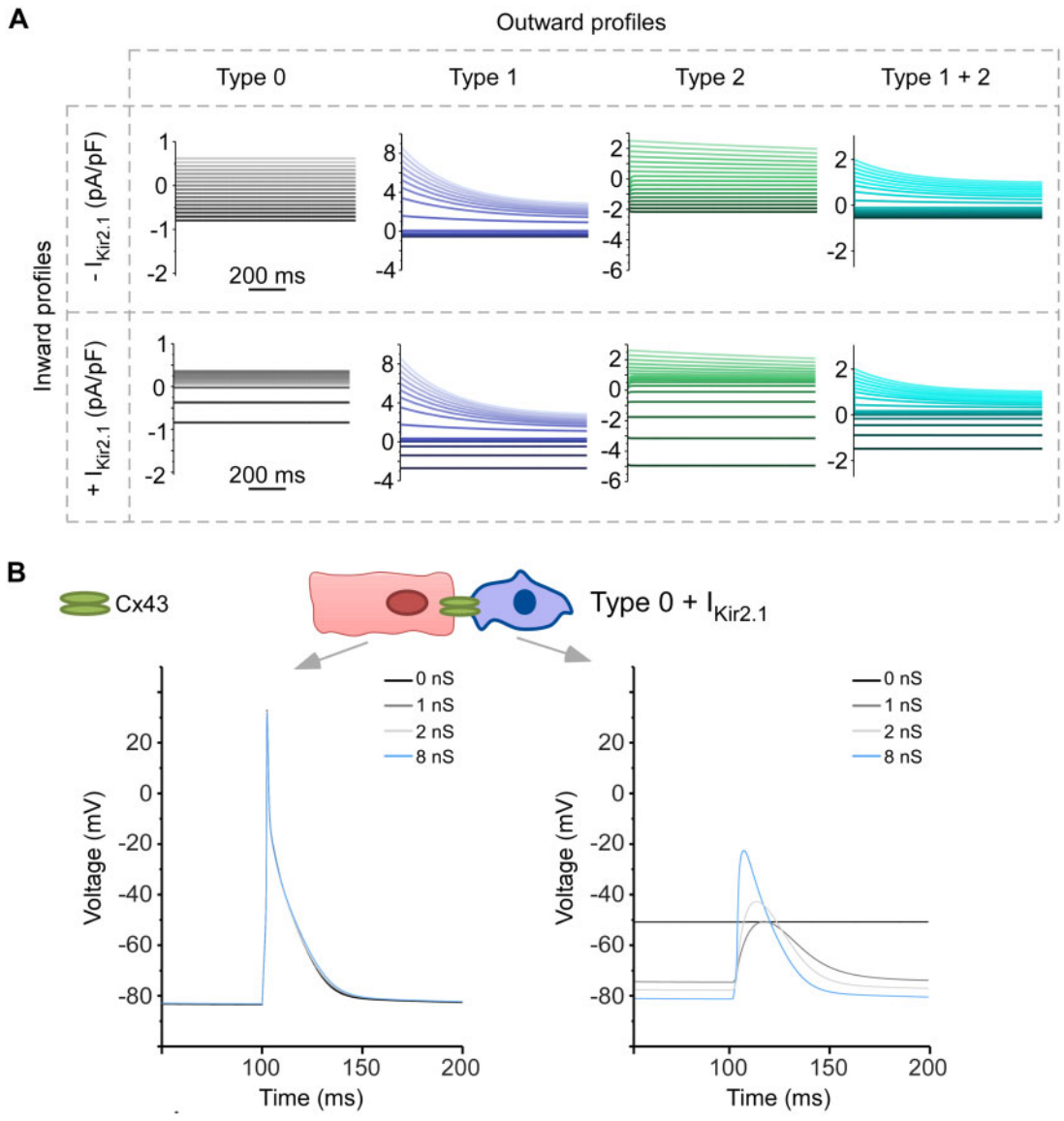

Figure 5 Modelling heterocellular MΦ–CM coupling: approach. (*A*) Simulated MΦ current profiles after applying the same voltage-clamp protocol as in *Figure 2B*, showing the different experimentally observed combinations that can be reproduced using the model. (*B*) Voltage dynamics of CM (left) coupled to MΦ (right, here Type 0 with inwardly rectifying current). Intercellular conductance was 0, 1, 2 or 8 nS. AP in CM were triggered by rectangular current pulses (2 ms, 5 nA).

small spherical cells (average surface area 379±22 μm^2), cultured MΦ are more elongated with cellular protrusions and a more than two-fold larger surface (841±103 μm^2). MΦ *in situ* display even more complex morphologies, with cellular branches that wrap around neighbouring CM, and an average surface area three times larger than freshly isolated cells (1,163±81 μm^2) (*Figure 1A and B*). The here observed cell surface values are significantly higher than those previously reported for murine cardiac MΦ in the AV node region (149±24 μm^2, Hulsmans *et al.*, 2017), where (erroneously) the cell cross-sectional area was referred to as cell 'surface'. Differences between freshly isolated, cultured, and *in situ* cells can be explained by the fact that cell isolation involves enzymatic digestion and mechanical agitation, apparently resulting in a loss of cellular protrusions (only cell fragments containing a nucleus may survive). The *in situ* MΦ morphology, 3D-reconstructed from optically cleared myocardium, allows the most appropriate means of evaluating cellular geometry and size in native tissue. This information is useful for scaling electrophysiological properties recorded from isolated and/or cultured MΦ towards values required for quantitative exploration of putative heterocellular electrical interactions in intact myocardium.

4.2 MΦ size correlates with passive electrophysiological properties

Our study provides first detail on the electrophysiological characterization of resident ventricular MΦ in mouse heart. Matching the observed increase in surface area, cultured MΦ had a 1.9-fold higher capacitance compared to freshly isolated MΦ (34±0.4 pF vs. 18.3±0.1 pF, $P<0.001$), while their membrane resistance was reduced by an inverse multiplier

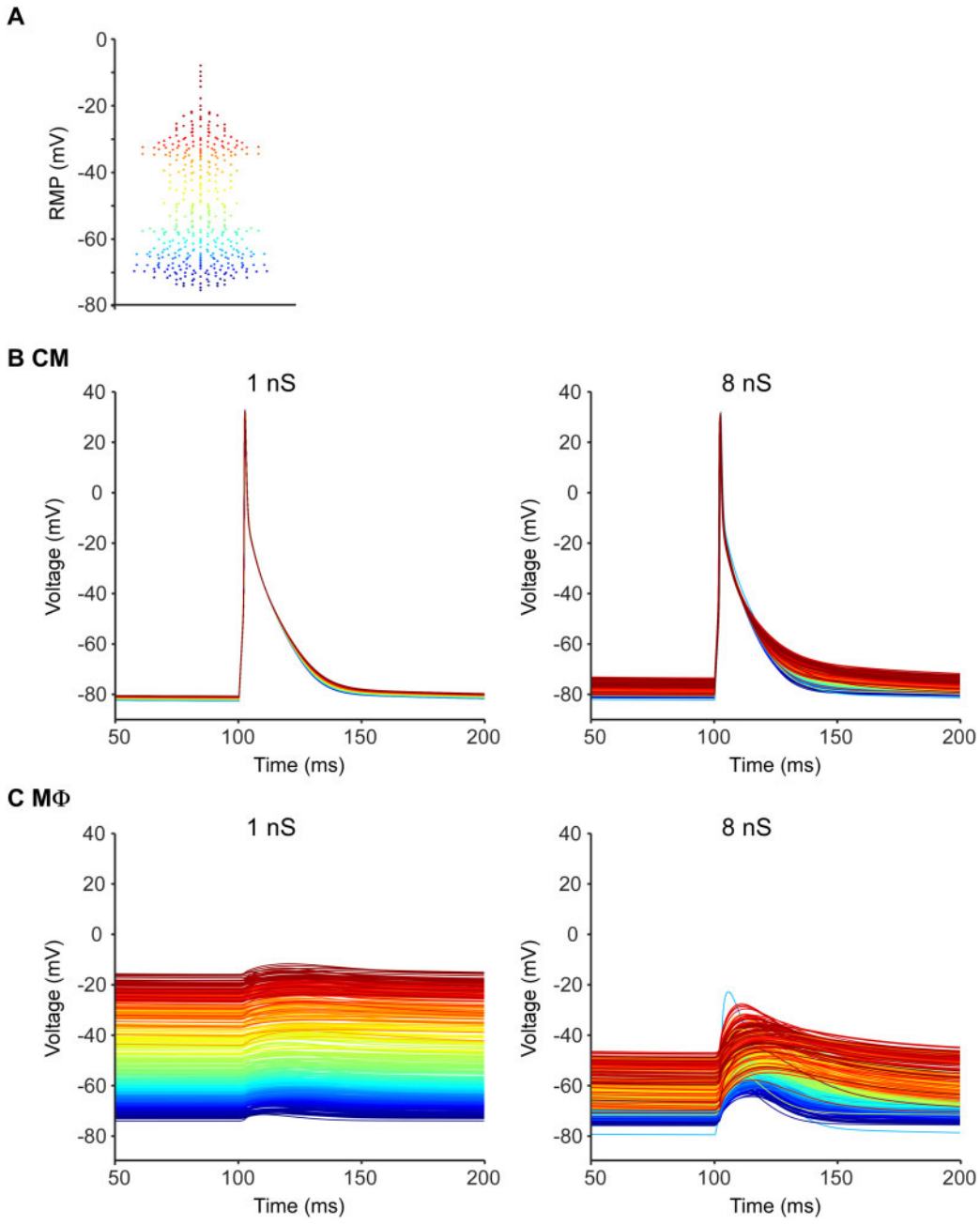

Figure 6 Modelling heterocellular MΦ–CM coupling: population of models. (*A*) Simulated RMP from isolated MΦ, colour coded according to MΦ RMP, as shown. (*B*) CM AP after coupling by a conductance of 1 nS (left) or 8 nS (right) to one of 400 MΦ, simulated in a population of models approach. (*C*) MΦ membrane potential after coupling them to a CM by a conductance of 1 nS (left) or 8 nS (right).

(0.51-fold: 1.12±0.03 GΩ vs. 2.21±0.07 GΩ, $P<0.001$). RMP did not change from isolation to one week of MΦ culture (*Figure 1B*).

If *in vitro* data can be scaled to the *in situ* setting, one would predict that tissue-resident MΦ have an average membrane capacitance of about 56 pF and a membrane resistance in the order of 720 MΩ. Accordingly, effects of MΦ on coupled CM might be underestimated *in vitro*, and *in silico* when relying on electrophysiological data from freshly isolated cells. To date, direct measurements of passive MΦ properties in tissue are lacking. Direct recordings *in situ* would be particularly challenging if MΦ were electrotonically coupled to other cell types, in particular CM. Such coupling, apparently *via* Cx43, is evident in mouse atrioventricular node,[8] and it is plausible elsewhere, as Cx43 was detected in over 90% of freshly isolated ventricular MΦ (*Figure 3J*). Further research is needed to explore the functional relevance of this facet of cardiac heterocellular electrophysiology, as discussed below.

4.3 Kv1.3, Kv1.5, and Kir2.1 are functionally expressed in cardiac MΦ

In addition to passive electrophysiological properties, we investigated voltage-activated currents in MΦ. We found four different patterns of

voltage-activated outward currents in isolated MΦ, both in the absence or presence of voltage-gated inwardly rectifying currents (*Figure 2B*). Ion selectivity experiments showed that underlying ion channels are predominantly K^+ selective (*Figure 1C and D*). Based on RNA-seq, immunocytochemical labelling, and pharmacological interventions, we identified Kv1.3, Kv1.5, and Kir2.1 as key ion channels responsible for the currents observed in cardiac MΦ (*Figures 1–3*). The *Kcng2* gene, found in RNA-seq data, encodes Kv6.2, which was not observed functionally. This channel has been classified previously as electrophysiologically silent, explaining its lack of detectable activity.[39] That said, Kv6.2 can form heteromers with Kv2.1 channels, modifying the voltage dependence of their activation and inactivation kinetics.[40] Our results are in line with previous studies showing that leukocytes express a diverse repertoire of Kv proteins, driving outward K^+ currents, incl. Kv1.3 and Kv1.5.[20,41,42] Several electrophysiological studies described inwardly rectifying currents and identified Kir channels as responsible for this current.[43–45] Our data establish that the inwardly rectifying K^+ channel Kir2.1 is functionally expressed in 52% of murine cardiac ventricular MΦ.

While this study focuses on voltage-gated K^+ channels, our RNA-seq data also indicate expression of a variety of other ion channels, incl. TRPV4, TRPM7, and TRPC3. This is in keeping with previous studies showing TRPV4 channel activity in murine MΦ of different origin (bone marrow-derived and alveolar MΦ).[46,47] Whether or not these channels are functionally expressed in the plasma membrane (or in intracellular organelles) of cardiac MΦ, and how they may be activated, needs to be explored in follow-up research. Our data suggests that the contribution of Ca^{2+} conducting channels to voltage-activated currents in MΦ is smaller than that of K^+ channels, and that Cl^- channels do not play a significant role in the observed whole-cell current profiles, at least using the here described experimental conditions.

It is unclear whether the heterogeneous current profiles observed in cardiac MΦ may be attributable to different states of MΦ activation (e.g. activated vs. quiescent MΦ), or linked to their origin (tissue-resident vs. recruited MΦ), as has been suggested for other types of MΦ.[42] Thus, the functional relevance of K^+ channel-based currents in cardiac MΦ remains to be elucidated. Also, the nature and activity of ion flux pathways for Na^+ and Ca^{2+} (in our computational models currently subsumed in the background current) needs to be evaluated further.

4.4 Electrotonically coupled MΦ can affect CM electrophysiology

The study of heterocellular electrotonic coupling in native myocardium *in situ* remains challenging. In this regard, cell-type-specific targeting of optogenetic reporters or actuators has opened up new ways to study cell–cell interactions.[48] Using a membrane potential reporter targeted to fibroblasts, Quinn *et al.*[11] demonstrated for the first time in 2016 that non-myocytes can electrotonically couple to CM in murine ventricular scar border zones *in situ*. This was subsequently confirmed by Rubart *et al.*[49] Using a light-activated ion channel targeted to MΦ, Hulsmans *et al.* showed in 2017 that resident cardiac MΦ can electrotonically couple to CM *via* Cx43-based junctions, and that this coupling affects AV node conduction in healthy murine heart. Using RNA-seq, we confirm that Cx43 is the dominant connexin isoform in cardiac resident MΦ (*Table 1*), and we show that it is expressed at the surface of the vast majority of isolated MΦ, as well as at points of heterocellular contact in tissue (*Figure 3K* and Supplementary *Figures S4 and S5*).

While it is widely accepted that conduction in working myocardium is maintained chiefly *via* Cx43-containing gap junctions between CM, it has been suggested that extensive membrane approximations (*via* capacitative effects), dynamic changes in the composition of the extracellular fluid in restricted spaces between cells (*via* ephaptic coupling),[50] or tunnelling nanotubes (which can interconnect different cells directly)[11,51] may also play a role in heterocellular electrophysiological interactions in the heart. Non-canonical mechanisms of CM–MΦ coupling are ill-explored and need to be investigated in follow-up studies involving 3D nanoscopic reconstruction of heterocellular contact sites, such as by EM tomography.[11] In addition, Cx43 expression at points of contact between CM and MΦ, observed by us and others,[8] may have other intriguing functions (apart from electrotonic coupling), including structural roles and contributions to inflammatory signalling.[52]

Based on our experimental findings, we established a computational model incorporating measured passive electrophysiological properties and three ion conductances to describe different types of MΦ behaviour observed (*Figures 4 and 5A*). This was used to quantitatively assess the plausibility of effects of MΦ–CM coupling on RMP of the two cell types and, in CM, on AP dynamics (*Figure 5B*). Note that, these simulations are based on the premise that MΦ are coupled to CM in native tissue—a stipulation that has yet to be confirmed directly for tissue outside the murine AV node.

Using a population of models approach, whereby key ion currents and capacitance of MΦ, as well as their coupling to CM, are systematically varied, we found that MΦ can depolarize RMP of CM with increased MΦ coupling while, as expected, CM hyperpolarize RMP of MΦ upon electrotonic connection. Coupled MΦ follow rhythmic CM depolarizations upon AP generation, with more pronounced depolarizations of MΦ at higher coupling strengths (*Figures 5 and 6*). In turn, our models predict that MΦ affect the AP in coupled CM, shortening APD_{50} by up to 34.9% and prolonging APD_{90} by up to 12.7% in the most critical scenarios (*Figure 6*). Altogether, the numerical simulations identify heterocellular coupling strength along with MΦ RMP (which, in turn, is strongly affected by the absence or presence of the inward-rectifier $I_{Kir2.1}$, Supplementary *Figure S6*) as governing variables of MΦ effects on CM. Unsurprisingly, given the nature of active and passive electrophysiological properties, these effects are much less pronounced than those of CM on MΦ RMP.

Our results, combining original experimental and modelling data, suggest a very limited effect of MΦ on cardiac electrophysiology in intact (healthy) mouse ventricles (note that previously reported effects of MΦ on atrioventricular CM function[8] were driven by targeted light-activation of *non-native* channelrhodopsins in MΦ). This is in keeping with the idea that cardiac MΦ are mobile cells whose location and contact to individual CM is thought to be dynamic: if their coupling to CM had a major impact on individual CM excitability, it is likely that this would counter maintenance of a physiological steady-state.

Effects of MΦ on CM electrophysiology may differ in injured myocardium, e.g. following ischemia/reperfusion injury, when MΦ locally proliferate and/or infiltrate, thereby increasing the likelihood that multiple MΦ are coupled to one-another and/or to remaining CM in scar centre or border zones. This forms a worthwhile target for further investigation.

The here presented study provides a first characterization of the electrophysiology of resident cardiac MΦ, and a computational model which allows one to quantitatively assess putative electrophysiological consequences of heterocellular MΦ–CM coupling. Follow-on studies are needed to explore the presence of ion currents with different selectivity

(e.g. conducting Na^+ or Ca^{2+}) and mode of activation (e.g. ligand or mechanically activated channels), and to address canonical and non-canonical MΦ functions and their electrophysiological modulation in healthy and diseased myocardium.

Supplementary material

Supplementary material is available at *Cardiovascular Research* online.

Conflict of interest: none declared.

Funding

This study was supported by a 'la Caixa' Foundation (ID 100010434) PhD Fellowship (LCF/BQ/DR19/11740029 to A.S.-C.); a Berta-Ottenstein-Programme award for Advanced Clinician Scientists (to A.L.), two German Research Foundation Emmy-Noether Fellowships (DFG#265188911 to I.H., DFG#412853334 to F.S.-W.), a German Research Foundation research grant (DFG#183027722 to G.S.), and the European Research Council advanced grant CardioNect (to P.K.). The investigators are members of the German Research Foundation Collaborative Research Centre 1425 (DFG #422681845).

Acknowledgements

We thank Stefanie Feliz-Perez and Cinthia Walz for excellent technical support, and all members of the Institute for Experimental Cardiovascular Medicine (IEKM) for advice and critical discussions of the manuscript. We thank the SCI-MED facility at IEKM for access to and support with confocal microscopy; the Lighthouse Facility of the University of Freiburg for providing access and support for cell sorting; and the Freiburg Galaxy Team: Anika Erxleben and Prof Rolf Backofen, Bioinformatics, University of Freiburg, Germany (funded by Collaborative Research Centre 992 grant (DFG#192904750)). We acknowledge Dr Said El-Haou from Metrion for kindly providing the compound XEN-D0103.

Data availability

Data available on request. The macrophage electrophysiology model (including population model) is available in the CellML Model Repository at https://models.physiomeproject.org/workspace/638. All other codes (coupling model, image analysis algorithm) will be provided by the authors on request.

References

1. Pinto AR, Ilinykh A, Ivey MJ, Kuwabara JT, D'antoni ML, Debuque R, Chandran A, Wang L, Arora K, Rosenthal NA, Tallquist MD. Revisiting cardiac cellular composition. *Circ Res* 2016;**118**:400–409.
2. Adler CP, Ringlage WP, Böhm N. DNS-Gehalt und Zellzahl in Herz und Leber von Kindern. Vergleichende biochemische, cytophotometrische und histologische Untersuchungen. *Pathol Res Pract* 1981;**172**:25–41.
3. Heidt T, Courties G, Dutta P, Sager HB, Sebas M, Iwamoto Y, Sun Y, Da Silva N, Panizzi P, van der Laan AM, Swirski FK, Weissleder R, Nahrendorf M. Differential contribution of monocytes to heart macrophages in steady-state and after myocardial infarction. *Circ Res* 2014;**115**:284–295.
4. Epelman S, Lavine KJ, Randolph GJ. Origin and functions of tissue macrophages. *Immunity* 2014;**41**:21–35.
5. Dick SA, Macklin JA, Nejat S, Momen A, Clemente-Casares X, Althagafi MG, Chen J, Kantores C, Hosseinzadeh S, Aronoff L, Wong A, Zaman R, Barbu I, Besla R, Lavine KJ, Razani B, Ginhoux F, Husain M, Cybulsky MI, Robbins CS, Epelman S. Self-renewing resident cardiac macrophages limit adverse remodeling following myocardial infarction. *Nat Immunol* 2019;**20**:29–39.
6. Pinto AR, Godwin JW, Rosenthal NA. Macrophages in cardiac homeostasis, injury responses and progenitor cell mobilisation. *Stem Cell Res* 2014;**13**:705–714.
7. Nicolás-Ávila JA, Lechuga-Vieco AV, Esteban-Martínez L, Sánchez-Díaz M, Díaz-García E, Santiago DJ, Rubio-Ponce A, Li JL, Balachander A, Quintana JA, Martínez-de-Mena R, Castejón-Vega B, Pun-García A, Través PG, Bonzón-Kulichenko E, García-Marqués F, Cussó L, A-González N, González-Guerra A, Roche-Molina M, Martin-Salamanca S, Crainiciuc G, Guzmán G, Larrazabal J, Herrero-Galán E, Alegre-Cebollada J, Lemke G, Rothlin CV, Jimenez-Borreguero LJ, Reyes G, Castrillo A, Desco M, Muñoz-Cánoves P, Ibáñez B, Torres M, Ng LG, Priori SG, Bueno H, Vázquez J, Cordero MD, Bernal JA, Enríquez JA, Hidalgo A. A network of macrophages supports mitochondrial homeostasis in the heart. *Cell* 2020;**183**:94–109.e23.
8. Hulsmans M, Clauss S, Xiao L, Aguirre AD, King KR, Hanley A, Hucker WJ, Wülfers EM, Seemann G, Courties G, Iwamoto Y, Sun Y, Savol AJ, Sager HB, Lavine KJ, Fishbein GA, Capen DE, Da Silva N, Miquerol L, Wakimoto H, Seidman CE, Seidman JG, Sadreyev RI, Naxerova K, Mitchell RN, Brown D, Libby P, Weissleder R, Swirski FK, Kohl P, Vinegoni C, Milan DJ, Ellinor PT, Nahrendorf M. Macrophages facilitate electrical conduction in the heart. *Cell* 2017;**169**:510–522.e20.
9. Goshima K, Tonomura Y. Synchronized beating of embryonic mouse myocardial cells mediated by FL cells in monolayer culture. *Exp Cell Res* 1969;**56**:387–392.
10. Rook MB, Ginneken AV, Jonge BD, Aoumari AE, Gros D, Jongsma HJ. Differences in gap junction channels between cardiac myocytes, fibroblasts, and heterologous pairs. *Am J Physiol* 1992;**263**:C959–77.
11. Quinn TA, Camelliti P, Rog-Zielinska EA, Siedlecka U, Poggioli T, O'Toole ET, Knöpfel T, Kohl P. Electrotonic coupling of excitable and nonexcitable cells in the heart revealed by optogenetics. *Proc Natl Acad Sci USA* 2016;**113**:14852–14857.
12. Sachse FB, Moreno AP, Abildskov JA. Electrophysiological modeling of fibroblasts and their interaction with myocytes. *Ann Biomed Eng* 2008;**36**:41–56.
13. Maleckar MM, Greenstein JL, Giles WR, Trayanova NA. Electrotonic coupling between human atrial myocytes and fibroblasts alters myocyte excitability and repolarization. *Biophys J* 2009;**97**:2179–2190.
14. MacCannell KA, Bazzazi H, Chilton L, Shibukawa Y, Clark RB, Giles WR. A mathematical model of electrotonic interactions between ventricular myocytes and fibroblasts. *Biophys J* 2007;**92**:4121–4132.
15. Kohl P, Kamkin A, Kiseleva I, Noble D. Mechanosensitive fibroblasts in the sino-atrial node region of rat heart: interaction with cardiomyocytes and possible role. *Exp Physiol* 1994;**79**:943–956.
16. Parkhurst CN, Yang G, Ninan I, Savas JN, Yates JR, Lafaille JJ, Hempstead BL, Littman DR, Gan W-B. Microglia promote learning-dependent synapse formation through BDNF. *Cell* 2013;**155**:1596–1609.
17. Yona S, Kim K-W, Wolf Y, Mildner A, Varol D, Breker M, Strauss-Ayali D, Viukov S, Guilliams M, Misharin A, Hume DA, Perlman H, Malissen B, Zelzer E, Jung S. Fate mapping reveals origins and dynamics of monocytes and tissue macrophages under homeostasis. *Immunity* 2013;**38**:79–91.
18. Madisen L, Mao T, Koch H, Zhuo JM, Berenyi A, Fujisawa S, Hsu YWA, Garcia AJ, Gu X, Zanella S, Kidney J, Gu H, Mao Y, Hooks BM, Boyden ES, Buzsáki G, Ramirez JM, Jones AR, Svoboda K, Han X, Turner EE, Zeng H. A toolbox of Cre-dependent optogenetic transgenic mice for light-induced activation and silencing. *Nat Neurosci* 2012;**15**:793–802.
19. Fernández MC, Kopton RA, Simon-Chica A, Madl J, Hilgendorf I, Zgierski-Johnston CM, Schneider-Warme F. Channelrhodopsins for cell-type specific illumination of cardiac electrophysiology. *Methods Mol Biol* 2021;**2191**:287–307.
20. Beeton C, Wulff H, Barbaria J, Clot-Faybesse O, Pennington M, Bernard D, Cahalan MD, Chandy KG, Beraud E. Selective blockade of T lymphocyte K^+ channels ameliorates experimental autoimmune encephalomyelitis, a model for multiple sclerosis. *Proc Natl Acad Sci USA* 2001;**98**:13942–13947.
21. Afgan E, Baker D, Batut B, M Van Den B, Bouvier D, Ech M, Chilton J, Clements D, Coraor N, Grüning BA, Guerler A, Hillman-Jackson J, Hiltemann S, Jalili V, Rasche H, Soranzo N, Goecks J, Taylor J, Nekrutenko A, Blankenberg D. The Galaxy platform for accessible, reproducible and collaborative biomedical analyses: 2018 update. *Nucleic Acids Res* 2018;**46**:W537–W544.
22. Dobin A, Davis CA, Schlesinger F, Drenkow J, Zaleski C, Jha S, Batut P, Chaisson M, Gingeras TR. STAR: ultrafast universal RNA-seq aligner. *Bioinformatics* 2013;**29**:15–21.
23. Trapnell C, Williams BA, Pertea G, Mortazavi A, Kwan G, Baren MV, Salzberg SL, Wold BJ, Pachter L. Transcript assembly and quantification by RNA-Seq reveals unannotated transcripts and isoform switching during cell differentiation. *Nat Biotechnol* 2010;**28**:511–515.
24. S Van Der W, Schönberger JL, Nunez-Iglesias J, Boulogne F, Warner JD, Yager N, Gouillart E, Yu T. Scikit-image: image processing in python. *PeerJ* 2014;**2**:e453.
25. Lewiner T, Lopes H, Vieira AW, Tavares G. Efficient implementation of marching cubes' cases with topological guarantees. *J Graph Tools* 2003;**8**:1–15.
26. Schroeder W, Martin K, Lorensen B. The visualization toolkit: an object oriented approach to 3D graphics. *J Aust Entomol Soc* 1996;**34**:335–342.
27. Iyer V, Mazhari R, Winslow RL. A computational model of the human left-ventricular epicardial myocyte. *Biophys J* 2004;**87**:1507–1525.
28. Hou P, Zhang R, Liu Y, Feng J, Wang W, Wu Y, Ding J. Physiological role of Kv1.3 channel in T lymphocyte cell investigated quantitatively by kinetic modeling. *PLoS One* 2014;**9**:e89975.

29. Koivumäki JT, Seemann G, Maleckar MM, Tavi P. In silico screening of the key cellular remodeling targets in chronic atrial fibrillation. *PLoS Comput Biol* 2014;**10**:e1003620.
30. Britton OJ, Bueno-Orovio A, Ammel KV, Lu HR, Towart R, Gallacher DJ, Rodriguez B. Experimentally calibrated population of models predicts and explains intersubject variability in cardiac cellular electrophysiology. *Proc Natl Acad Sci USA* 2013;**110**: E2098–E2105.
31. Morotti S, Edwards AG, Mcculloch AD, Bers DM, Grandi E. A novel computational model of mouse myocyte electrophysiology to assess the synergy between Na^+ loading and CaMKII. *J Physiol* 2014;**592**:1181–1197.
32. Clerx M, Collins P, E de L, Volders PGA. Myokit: a simple interface to cardiac cellular electrophysiology. *Prog Biophys Mol Biol* 2016;**120**:100–114.
33. Hilgendorf I, Gerhardt LMS, Tan TC, Winter C, Holderried TAW, Chousterman BG, Iwamoto Y, Liao R, Zirlik A, Scherer-Crosbie M, Hedrick CC, Libby P, Nahrendorf M, Weissleder R, Swirski FK. Ly-$6C^{high}$ monocytes depend on nr4a1 to balance both inflammatory and reparative phases in the infarcted myocardium. *Circ Res* 2014;**114**: 1611–1622.
34. Epelman S, Lavine KJ, Beaudin AE, Sojka DK, Carrero JA, Calderon B, Brija T, Gautier EL, Ivanov S, Satpathy AT, Schilling JD, Schwendener R, Sergin I, Razani B, Forsberg EC, Yokoyama WM, Unanue ER, Colonna M, Randolph GJ, Mann DL. Embryonic and adult-derived resident cardiac macrophages are maintained through distinct mechanisms at steady state and during inflammation. *Immunity* 2014;**40**:91–104.
35. Spencer RH, Sokolov Y, Li H, Takenaka B, Milici AJ, Aiyar J, Nguyen A, Park H, Jap BK, Hall JE, Gutman GA, Chandy KG. Purification, visualization, and biophysical characterization of Kv1.3 tetramers. *J Biol Chem* 1997;**272**:2389–2395.
36. Loose S, Muller J, Wettwer E, El-Haou S, Jackson C, Tang R, Milnes J, Ravens U, Ford J. Positive frequency-dependent effects of highly selective Kv1.5 blockers (XEN-D0103 & MK-0448) in right atrial trabeculae from patients in sinus rhythm. *Circulation* 2013;**128**:18323.
37. Zhu XR, Wulf A, Schwarz M, Isbrandt D, Pongs O. Characterization of human Kv4.2 mediating a rapidly-inactivating transient voltage-sensitive K^+ current. *Recept Channels* 1999;**6**:387–400.
38. Camelliti P, Borg TK, Kohl P. Structural and functional characterisation of cardiac fibroblasts. *Cardiovasc Res* 2005;**65**:40–51.
39. Ranjan R, Logette E, Marani M, Herzog M, Tâche V, Scantamburlo E, Buchillier V, Markram H. A kinetic map of the homomeric voltage-gated potassium channel (Kv) family. *Front Cell Neurosci* 2019;**13**:358.
40. Bocksteins E, Snyders DJ. Electrically silent Kv subunits: their molecular and functional characteristics. *Physiology (Bethesda)* 2012;**27**:73–84.
41. Villalonga N, David M, Bielanska J, Vicente R, Comes N, Valenzuela C, Felipe A. Immunomodulation of voltage-dependent K^+ channels in macrophages: molecular and biophysical consequences. *J Gen Physiol* 2010;**135**:135–147.
42. Vicente R, Escalada A, Villalonga N, Texido L, Roura-Ferrer M, Martín-Satué M, López-Iglesias C, Soler C, Solsona C, Tamkun MM, Felipe A. Association of Kv1.5 and Kv1.3 contributes to the major voltage-dependent K^+ channel in macrophages. *J Biol Chem* 2006;**281**:37675–37685.
43. Moreno C, Prieto P, Macías Á, Pimentel-Santillana M, de la Cruz A, Través PG, Boscá L, Valenzuela C. Modulation of voltage-dependent and inward rectifier potassium channels by 15-Epi-Lipoxin-A4 in activated murine macrophages: implications in innate immunity. *J Immunol* 2013;**191**:6136–6146.
44. Randriamampita C, Trautmann A. Ionic channels in murine macrophages. *J Cell Biol* 1987;**105**:761–769.
45. Eder C, Fischer H-G. Effects of colony-stimulating factors on voltage-gated K^+ currents of bone marrow-derived macrophages. *Naunyn Schmiedebergs Arch Pharmacol* 1997;**355**:198–202.
46. Hamanaka K, Jian M-Y, Townsley MI, King JA, Liedtke W, Weber DS, Eyal FG, Clapp MM, Parker JC. TRPV4 channels augment macrophage activation and ventilator-induced lung injury. *Am J Physiol Lung Cell Mol Physiol* 2010;**299**:L353–L362.
47. Scheraga RG, Abraham S, Niese KA, Southern BD, Grove LM, Hite RD, McDonald C, Hamilton TA, Olman MA. TRPV4 mechanosensitive ion channel regulates lipopolysaccharide-stimulated macrophage phagocytosis. *J Immunol* 2016;**196**:428–436.
48. Schneider-Warme F. The power of optogenetics. *Herzschrittmacherther Elektrophysiol* 2018;**29**:24–29.
49. Rubart M, Tao W, Lu XL, Conway SJ, Reuter SP, Lin SF, Soonpaa MH. Electrical coupling between ventricular myocytes and myofibroblasts in the infarcted mouse heart. *Cardiovasc Res* 2018;**114**:389–400.
50. Veeraraghavan R, Poelzing S, Gourdie RG. Intercellular electrical communication in the heart: a new, active role for the intercalated disk. *Cell Commun Adhes* 2014;**21**: 161–167.
51. Wang X, Gerdes HH. Long-distance electrical coupling via tunneling nanotubes. *Biochim Biophys Acta* 2012;**1818**:2082–2086.
52. Yuan D, Wang Q, Wu D, Yu M, Zhang S, Li L, Tao L, Harris AL. Monocyte-endothelial adhesion is modulated by Cx43-stimulated ATP release from monocytes. *Biochem Biophys Res Commun* 2012;**420**:536–541.

Translational perspective

Cardiac tissue contains resident macrophages (MΦ) which, beyond immunological and housekeeping roles, have been found to electrotonically couple *via* connexins to cardiomyocytes (CM), stabilizing atrioventricular conduction at high excitation rates. Here, we characterize structure and electrophysiological function of murine cardiac MΦ and provide a computational model to quantitatively probe the potential relevance of MΦ–CM coupling for cardiac electrophysiology. We find that MΦ are unlikely to have major electrophysiological effects in normal tissue, where they would hasten early and slow late CM-repolarization. Further work will address potential arrhythmogenicity of MΦ in patho-physiologically remodelled tissue containing elevated MΦ-numbers, incl. non-resident recruited cells.